Epitaxial growth and atomic-scale study of type-II Dirac semimetal 1*T*-$NiTe_2$ film

Mingqiang Ren,[1,2,*] Shuze Wang,[2] Fanqi Meng,[3] Lixuan Wei,[2] Qinghua Zhang,[3] Lin Gu,[4] Can-Li Song,[2,5,†] Xu-Cun Ma,[2,5,‡] and Qi-Kun Xue[1,2,5,6]

[1]*Shenzhen Institute for Quantum Science and Engineering and Department of Physics, Southern University of Science and Technology, Shenzhen 518055, China*

[2]*State Key Laboratory of Low-Dimensional Quantum Physics, Department of Physics, Tsinghua University, Beijing 100084, China*

[3]*Beijing National Laboratory for Condensed Matter Physics, Institute of Physics, Chinese Academy of Sciences, Beijing 100190, China*

[4]*Beijing National Center for Electron Microscopy and Laboratory of Advanced Materials, Department of Materials Science and Engineering, Tsinghua University, Beijing 100084, China*

[5]*Frontier Science Center for Quantum Information, Beijing 100084, China*

[6]*Beijing Academy of Quantum Information Sciences, Beijing 100193, China*

(Received 11 August 2023; revised 16 October 2023; accepted 21 November 2023; published 6 December 2023)

By means of molecular beam epitaxy, x-ray diffraction, transmission electron microscopy, and *in situ* scanning tunneling microscopy, we successfully prepare type-II Dirac semimetal 1*T*−$NiTe_2$ films and investigate their surface morphology, electronic structure, and topological characteristics on the atomic scale. Atomically flat $NiTe_2$ films can be readily prepared on $SrTiO_3$(001) substrates at ∼210 °C. For $NiTe_2$ multilayers (∼17 layers), the predominant surface defect is identified as intercalated Ni atoms inside the van der Waals gap. Besides, we observe spin-splitting and resonant topological surface states near E_F and at ~ -0.65 eV, respectively. They are suppressed at the step edges and in ultrathin monolayer and bilayer films. By exploring the quasiparticle interference, we visualize a backscattering suppression within 140 ± 40 meV in multilayer $NiTe_2$, which is associated possibly with the type-II Dirac node.

DOI: 10.1103/PhysRevB.108.235408

I. INTRODUCTION

Layered transition metal dichalcogenides (TMDCs) with nontrivial topology and quantum orders have attracted wide attention in condensed matter physics for exploring exotic quantum phenomena [1]. Recently, a new quantum phase, the type-II Dirac semimetal (DSM) has been identified in some of the group VIII-VIIA based dichalcogenides 1*T*−MX_2 (M = Pd, Pt, Ni; X = Se, Te) [2–17]. In sharp contrast, in the type-I DSMs such as Na_3Bi [18,19], Cd_3As_2 [20–23], and $ZrTe_5$ [24], the low-energy excitations of Dirac fermions in type-II DSMs are not protected by the Lorentz symmetry, generating strongly tilted bulk Dirac nodes (DPs) along the [001] direction [2–4]. The Lorentz symmetry breaking gives rise to a variety of novel phenomena, such as the anisotropic magnetoresistance, angle-dependent chiral anomaly, topological Lifshitz transition, and topological superconductivity [2–5,17,25,26].

Among all the type-II DSMs, 1*T*−$NiTe_2$ exhibits a DP ($-20 \sim 80$ meV) closest to the Fermi energy (E_F) [11–17], compared to that in $PdTe_2$ (~ -0.6 eV [5–7]), $PtTe_2$ (~ -0.8 eV [8,9]), and $PtSe_2$ (~ -1.2 eV [5,10]). Besides, the energy or momentum position of the DP exhibits strong tunability with strain or alkali metal intercalation [5,27]. These properties make $NiTe_2$ an improved platform to study the physics of the relativistic Dirac fermion and its entanglement with competed orders, and to develop spintronic or topological electronic devices [5–13,17]. Up to now, the topological characteristics of $NiTe_2$ are routinely characterized by quantum oscillations and angle-resolved photoemission spectroscopy (ARPES) in momentum space [11–16]. Complementary, scanning tunneling microscopy/spectroscopy (STM/S) study in real space on the atomic scale is quite rare. Previous STM investigations of $NiTe_2$ or other type-II DSMs mainly focus on the surface defects [28–35]. Motivated by this, we explored the electronic states and the quasiparticle interferences (QPIs) associated with the topological surface states (TSSs) and DPs in $NiTe_2$ films using spectroscopic-imaging STM.

As shown in the upper panel of Fig. 1(a), 1*T*−$NiTe_2$ crystallizes into a hexagonal CdI_2-type structure with a space group $P\bar{3}m1$. The two-dimensional (2D) Te-Ni-Te triple layers (TLs), which are composed of hexagonally packed Ni atoms sandwiched between two layers of Te, are vertically bonded via a weak van der Waals (vdW) force and thus can be easily prepared as ultrathin films. Previously, $NiTe_2$ films have been synthesized on several substrates, such as on graphene/SiC and GaAs via molecular beam epitaxy (MBE) [36,37] or on mica, HOPG, SiO_2/Si, and MoS_2 by chemical vapor deposition (CVD) [28,38,39]. In our work, we prepared $NiTe_2$ films on Nb-doped $SrTiO_3$(001) (STO hereafter) substrate via MBE. Here, Nb doping makes the $SrTiO_3$ substrate metallic to conduct the STM tunneling current.

II. EXPERIMENTAL DETAILS

MBE and STM measurements were performed in a commercial STM facility (USM-1500 from UNISOKU Co., Ltd.).

*renmq@sustech.edu.cn
†clsong07@mail.tsinghua.edu.cn
‡xucunma@mail.tsinghua.edu.cn

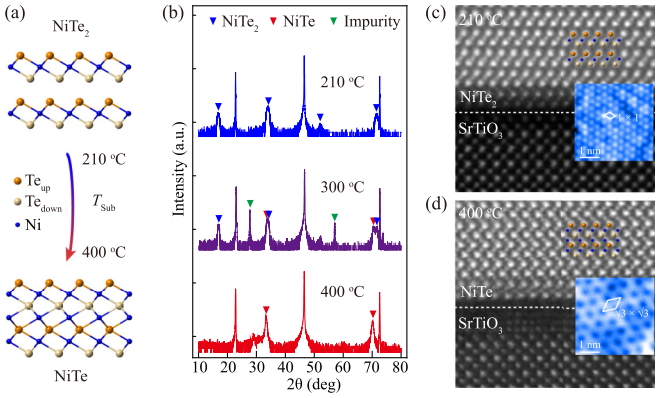

FIG. 1. (a) Sketched crystal structure and T_{sub}-controlled MBE growth of $1T-NiTe_2$ on STO. (b) XRD patterns of as-grown films with a nominal thickness of 17 TL at varied T_{sub} as labeled. (c), (d) High-resolution TEM images of $NiTe_2$ (210 °C) and NiTe (400 °C) films (∼17 TL) near the interface with corresponding lattices superimposed for clarity. Insets show the atomically resolved STM images away from defects revealing the 1×1 and $\sqrt{3} \times \sqrt{3}$ surface structures of $NiTe_2$ and NiTe, respectively.

Before growth, STO substrates (wt 0.7%) were annealed to 1200 °C to obtain an atomically flat surface. High-purity Ni (99.99%) and Te (99.999%) were then co-evaporated from standard Knudsen diffusion cells. After growth, $NiTe_2$ films were immediately transferred into the STM module and all STM/S measurements were performed at 4.5 K. Polycrystalline PtIr tips were calibrated on Ag/Si(111) films and used throughout the experiments. For ultrathin $NiTe_2$, the thickness was determined from the relative terrace height with STO substrate, whereas for the multilayer film, a nominal thickness was estimated from the deposition flux and duration. All STM topographies were acquired in a constant current mode. dI/dV spectroscopy and dI/dV maps were measured using a standard lock-in technique with a small ac modulation V_{mod} at a frequency of $f = 645$ Hz. X-ray diffraction (XRD) was performed using a monochromatic Cu Kα1 radiation with a wavelength of 1.5406 Å. The cross-section TEM lamella sample was prepared utilizing a focused ion beam (FEI, Helios 600i) method where the lamella was thinned and polished using an 8 kV ion beam followed by removal of the amorphous damaged layer with a 5 kV ion beam. The TEM characterization was conducted using a Cs-corrected STEM (JEOL, ARM200CF) operating at 200 kV. HAADF-STEM images were obtained with a collection semiangle ranging from 90 to 370 mrad.

III. RESULTS AND DISCUSSION

We begin our study with the growth dynamics of $NiTe_2$ on STO substrate. Figure 1(b) shows the x-ray diffraction (XRD) patterns of as-grown films (∼17 TL) at varied substrate temperatures (T_{sub}). A crystallinity of $1T-NiTe_2$ film is realized at 210 °C, as demonstrated by the topmost blue curve. One can see that all the diffraction peaks are assigned to the (00n) planes of $NiTe_2$ without any impurity phase. The c-axis lattice constant of our MBE-prepared film is calculated to be 5.278 ± 0.005 Å. We note that this value is slightly larger (∼3‰) than that of the stoichiometric $NiTe_2$, but is consistent with that of the intercalated $Ni_{1+x}Te_2$ with a dilute Ni intercalation ($x < 0.03$) [11,38,40,41]. It is worth mentioning that the intercalation is very weak and is invisible in the transmission electron microscopy (TEM) image for thickness above 2 TL, as shown in Fig. 1(c). Besides, the TEM image reveals a periodic stacking of Te-Ni-Te trilayers, consistent with the (0001)-oriented $1T-NiTe_2$. This is also confirmed by the atomically resolved STM image inserted in Fig. 1(c) which reveals a Te-terminated hexagonal lattice with an in-plane lattice constant of $\sim 3.8 \pm 0.1$ Å. No reconstruction or charge modulation is observed on the surface, consistent with previous reports [28–30].

We note that T_{sub} have a significant effect on the growth behavior of $NiTe_2$ films on STO. With T_{sub} increasing to 400 °C, the film crystallizes into a NiAs-type NiTe lattice with a space group $P63/mmc$ as shown by the red curve in Fig. 1(b). At an intermediate $T_{sub} \sim 300$ °C, $1T-NiTe_2$, NiTe and some other impurity phases coexist in the film (purple curve). In sharp contrast to $1T-NiTe_2$, the TEM image of NiTe reveals an alternatively stacking of -(Ni-Te)- and a missing vdW gap, as shown in Fig. 1(d). Moreover, the topmost surface of NiTe reconstructs into a $\sqrt{3} \times \sqrt{3}$ superlattice with a periodicity of ∼6.5 Å, as shown in the inset of Fig. 1(d). This reconstruction stems from the Te-Ni covalent bonds at the surface.

Having clarified the growth dynamics, we focus on the $NiTe_2$ films prepared at 210 °C to investigate their surface morphology, electronic states, and QPI patterns. Figure 2(a) shows a large-area STM topographic image of such a film (∼17 TL), revealing a perfect layer-by-layer epitaxial growth. The film exhibits atomically flat terraces extending up to thousands of square nanometers, as shown in Fig. 2(b). Typically, there are two types of point defects in the film as labeled with A and B. Both have a threefold symmetry and locate at the hollow sites of the topmost Te atoms as demonstrated by the atomically resolved image in the inset.

The type-A defect is the predominant point defect and appears as a trefoil with a bright center in the empty states. In previous STM study [29], this defect has been assigned to the antisite Te_{Ni} in which the Te atom substitutes Ni. Inspired by our XRD measurements, we propose another possibility that this defect is the self-intercalated Ni atom (Ni_{inter}) within the vdW gap. If so, the intercalation introduces additional Ni atoms that would drive our film off-stoichiometric. From the topographic STM images, the areal density (n) of this defect is calculated to be $n \sim 1.84 \times 10^{13}/cm^2$, corresponding to 0.023 defect per unit cell. Considering a uniform intercalation of Ni inside the film for simplicity, the chemical composition of our film is estimated to be $Ni_{1.023}Te_2$. This small off-stoichiometry quantitatively explains the enlarged out-of-plane lattice constant of our film in Fig. 1(b) [40]. We note that the self-intercalation occurs very easily during the preparation of layered TMDC materials [42,43]. Compared to the CVD-synthesized films or bulk crystals [28,29], our film exhibits a larger density of Ni_{inter}, which arises probably from a lower Te evaporation pressure in our experiments. In stark contrast to type-A defect, the type-B defect exhibits a much lower density smaller than $2 \times 10^{11}/cm^2$. We assign this defect as the Te_{Ni} antisite defect or Ni vacancy considering its atomic registration.

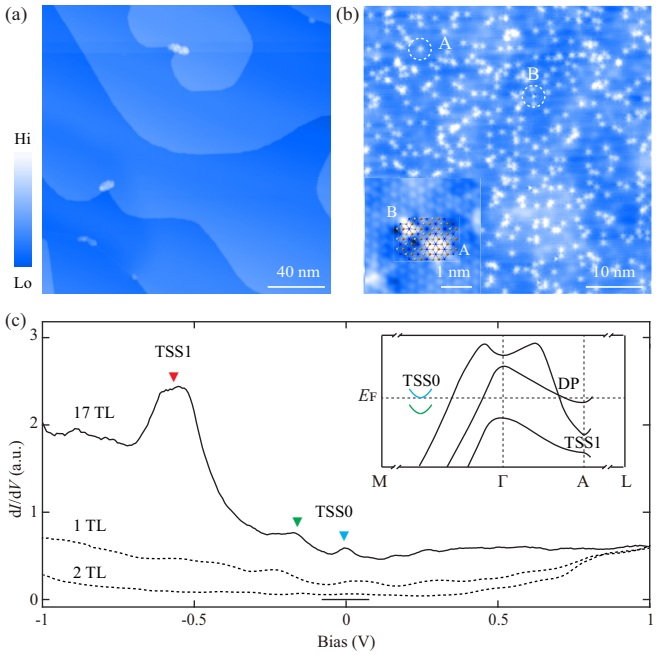

FIG. 2. (a), (b) Large- and small-area STM image (200 nm × 200 nm, $V = 3$ V, $I = 5$ pA; 50 nm × 50 nm, $V = 1$ V, $I = 500$ pA) of a 17 TL $NiTe_2$ film. Inset in (b) shows the atomically resolved images (10 nm × 10 nm, $V = 1$ V, $I = 500$ pA) revealing the registration of two types of native defects. (c) Typical dI/dV spectrum ($V = 1$ V, $I = 1$ nA, $V_{mod} = 20$ mV) measured on a defect-free area of 17 TL $NiTe_2$. Three distinct DOS peaks from TSS0 and TSS1 are marked by red, green, and cyan triangles, respectively. The dashed curves display the dI/dV spectra of 1 TL and 2 TL for comparison. Inset shows the sketched band structure of $NiTe_2$, emphasizing the topological surface states and the Dirac point.

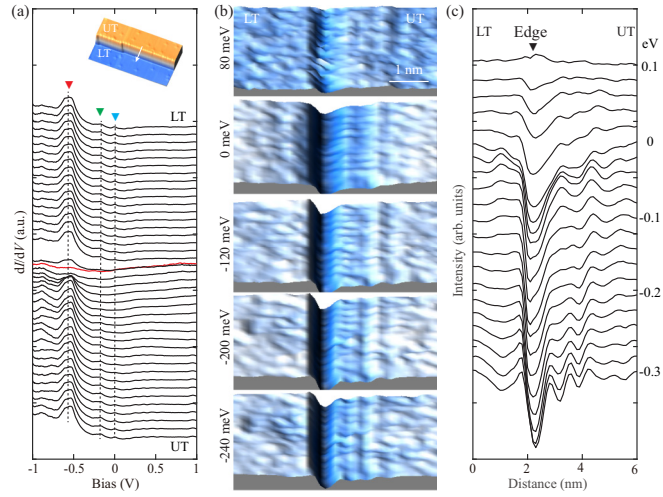

FIG. 3. (a) A series of dI/dV spectra measured across a step edge along the (100) direction of a 17 TL $NiTe_2$ film with a spacing of 2 Å. See the white arrow in the inset (30 nm × 15 nm, $V = 1$ V, $I = 30$ pA). The spectrum measured at the edge is colored in red. UT: Upper terrace; LT: lower terrace. (b) dI/dV maps measured at varied energies revealing the standing waves at the upper terrace. (c) Intensity line-cuts of the dI/dV maps across the step edge as a function of position. The line-cuts are integrated over a field of view of 6 nm × 3 nm along the width direction to eliminate the spatial inhomogeneity.

Figure 2(b) depicts a typical dI/dV spectrum acquired on a defect-free area of 17 TL $NiTe_2$, revealing multiple density of state (DOS) peaks. As reported previously [29], the two low-energy peaks at $\sim E_F$ (green triangle) and ~ -0.17 eV (cyan triangle) are from a spin-polarized topological surface state (TSS0 in inset). The spin splitting in our film is about 0.17 eV, slightly larger than that of ∼0.13 eV in the bulk [29]. Moreover, we observe another DOS peak with a width of 0.23 eV at ~ -0.65 eV (red triangle). By a comparison with ARPES results [12,13,15], this peak can be easily assigned to another topological surface state (TSS1) at a deeper binding energy. The enhanced intensity is due to the nature of the resonance state of TSS1 experiencing strong interaction with the bulk states [13]. As sketched in the Fig. 2(c) inset, TSS1 resides inside an inverted band gap (IBG) with inverted parities at the A point. The gap size of this IBG is thus expected to be larger than ∼0.23 eV, to wit the width of TSS1. Besides, the single peak feature signifies a weak spin splitting of TSS1.

These topological surface states, especially TSS1, disappear in monolayer (1 TL) and bilayer (2 TL) $NiTe_2$ as demonstrated by the dashed lines in Fig. 2(c). This reveals a collapse of the topological nature in $NiTe_2$/STO film at the two-dimensional (2D) limit, similar to that prepared on graphite SiC substrate [36]. Besides, TSS0 and TSS1 also get suppressed near the step edges which serve as surface scatterings, as shown in Fig. 3(a). Figures 3(b) and 3(c) show the low-energy dI/dV maps and corresponding intensity line-cut across the step edge at varied energies, revealing clearly the edge-driven standing waves on the upper terrace. The standing waves are more easily distinguished at negative energy when TSS0 develops. Moreover, the standing waves decay rapidly and fade away within a distance less than ∼3 nm off the step. The decay is much faster than that in ordinary 2D electron gas [44,45], but is comparable to that in topological insulators in which the unusual topological spin texture helps prohibit backscattering [46]. The fast decay of the standing waves near the step edge further demonstrates the topology nature of TSS0 from the STM perspective. To further explore the topology of $NiTe_2$, especially the type-II Dirac fermion near E_F, we measured the real-space dI/dV maps of 17 TL $NiTe_2$. The intercalated Ni atoms act as a perturbation to the surface potential, consequently serving as scattering centers to the QPI signal. Taking the zero-energy map shown in Fig. 4(a) as an example, Ni_{inter} induces a DOS suppression (dashed circle) surrounded by short-range standing waves. To get access to the scattering wave vectors q, we convert the voltage-dependent dI/dV maps into reciprocal space and show the resulting fast Fourier transform (FFT) images in Figs. 4(b)–4(h). Depending on the energy E, the FFT images exhibit multiple scatterings (labeled with q_1 to q_4) in the first Brillouin zone (BZ). To further reveal their evolutions, we plot in Fig. 4(i) the FFT intensity line-cut along Γ-K (right) and Γ-M (left) directions.

Band topology is a fundamental premise to understand the QPI patterns and associated scatterings. According to ARPES and theoretical calculations [11–17], there are two

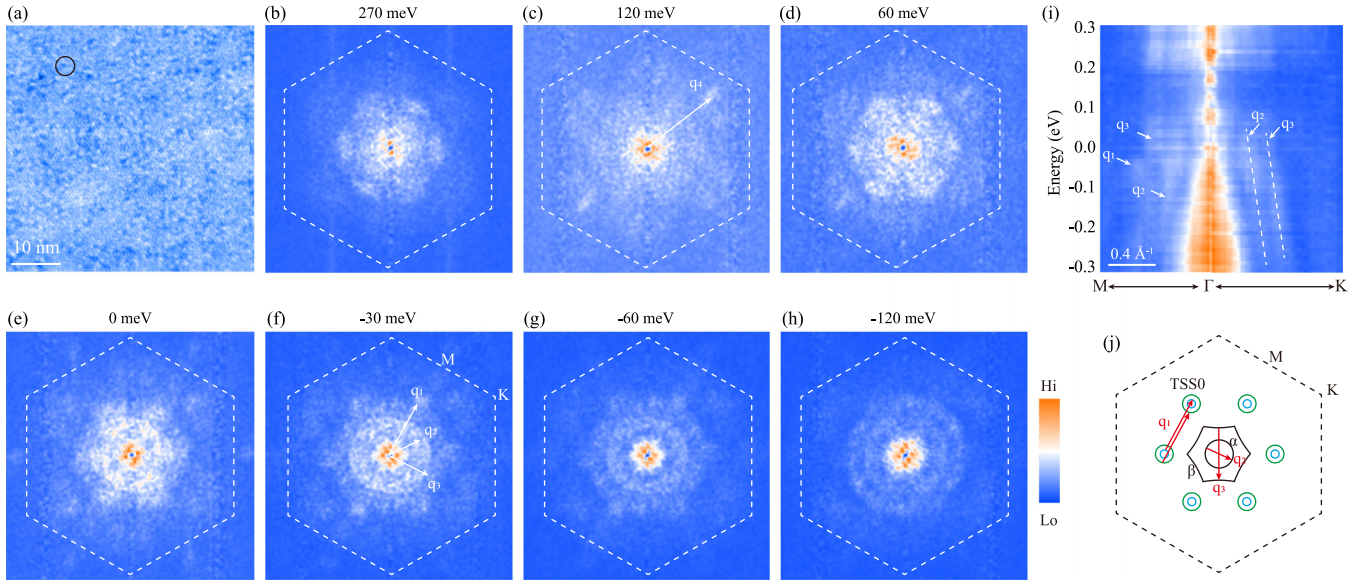

FIG. 4. (a) Typical dI/dV map (50 nm × 50 nm, $E = 0$ meV) taken on a 17 TL $NiTe_2$ film with the same field of view as Fig. 2(b). The black circle marks a single Ni_{inter} defect. [(b)–(h)] FFT images transformed from the dI/dV maps taken at varied energies as labeled. Four dominating scattering vectors are marked with q_1 to q_4. The white dashed hexagons sketch the first BZ. (i) Energy-dependent FFT intensity line-cut along Γ-K (right) and Γ-M (left) directions. The white dashed lines indicate the hole-like dispersion of q_2 and q_3, respectively. (k) Sketched Fermi surface contour of $NiTe_2$. The bulk α, β bands and spin-splitting TSS0 are colored in black, green, and blue, respectively. q_1 to q_3 mark the corresponding intraband scattering within TSS0, α, and β.

hole bands and two electron bands across E_F in $NiTe_2$. These bands contribute a complicated Fermi surface contour as shown in Fig. 4(j), consisting of a circular (α) and a hexagonal (β) hole pocket around Γ, as well as a forcipate-shaped (γ) and a dot-shaped (δ) electron pocket around the BZ boundary (not shown). Also, the spin-splitting TSS0 discussed above locates near E_F, contributing two electron-like pockets.

We begin our discussion with the FFT image at −30 meV [Fig. 4(f)], which exhibits three typical scatterings, including the sixfold spots (q_1), a ring (q_2), and a hexagon (q_3). q_1 can be assigned to the intraband scatterings of TSS0 for two reasons. First, q_1 shows up within only a small energy range from −0.1 eV to E_F with an electron-like dispersion, in parallel to the upper spin branch of TSS0. Second, q_1 locates at $q = 0.5$ Å^{-1} along Γ-M as shown in Figs. 4(f) and 4(i), matching well with the nearest-neighboring intraband scattering of TSS0 shown in Fig. 4(j). Note that the backscatterings between the six pockets of TSS0 are not observable in the FFT images, in analogy to the spin-texture induced backscattering suppression in topological insulators [47].

In contrast to energy-localized q_1, q_2 and q_3 disperse over the whole energy range measured (±300 meV). As shown in Figs. 4(e)–4(i), both q_2 and q_3 exhibit a hole-like dispersion below E_F. Together with their shapes, q_2 and q_3 are easily assigned to the intraband scatterings of α and β as illustrated in Fig. 4(j). Considering the scattering geometry ($q = 2k$), the Fermi wave vectors k_F for α and β bands along the Γ-M direction are calculated to be ∼0.15 Å^{-1} and ∼0.23 Å^{-1}, quite consistent with reported ARPES measurements and theoretical calculations [11–17].

With increasing energy above E_F, the Te-5p derived α and β bands tend to touch each other as sketched in the Fig. 2(c) inset, generating a type-II bulk DP [11–13,15,17]. In our experiments, q_2 and q_3 are first suppressed within $E \sim 100$ meV to 180 meV and some spectral weight returns at higher energies, as shown in Figs. 4(b)–4(d) and 4(i). This suppression could originate from the spin-momentum locking of the type-II DP [2–4] and should be further confirmed by theoretical calculations. Supposing that the DP locates at the middle of the suppression region, its energy position (E_D) is estimated to be ∼140 meV in our films. At larger q around the BZ boundary, one may note the existence of some scattering features q_4 that seems to exhibit a twofold symmetry. They are related to the scatterings from the electron-like bands around K points [11–17] and the symmetry breaking needs further investigations.

We note that the DP energy of our $NiTe_2$ film is higher than the predicted one (−20 ∼ 80 meV) in theoretical calculations [11–15,17]. This deviation can be explained by considering an out-of-plane tensile strain, which decreases the overlap between the wave functions and lifts the DP energy with respect to E_F [27]. In our films, the tensile strain stems from Ni intercalation that tends to increase c. Thus, controlling the density of Ni_{inter} provides an effective way to engineering the DP energy or perhaps even its tilt parameters. Moreover, the discrepancy of the energy positions of DPs reported in bulk crystals [11–16] may also arise from the lattice alteration induced by the Ni intercalation.

At last, it is worth mentioning that no superconductivity is observed in our $NiTe_2$ films measured at 4.5 K regardless of the thickness. Considering that the emergent superconductivity in $NiTe_2$ crystals ubiquitously exhibits a very low T_c [48–51], further experiments at extremely low temperature are highly desirable. Besides, more suitable substrates such as graphene, which usually contributes

weak interfacial interaction [52,53], should be considered in further experiments to achieve the intrinsic two-gap superconductivity at the 2D limit [54].

IV. CONCLUSION

In summary, we successfully prepared $1T-NiTe_2$ film on Nb-$SrTiO_3$(001) substrate and investigated its topological characteristics using spectroscopic-imaging STM. Our measurements reveal several important aspects of multilayer $NiTe_2$ films (∼17 TL). First, the dominant surface defect is the Ni self-intercalation that modifies the c-axis lattice parameter in an extension way. Second, topological surface states survive down to 17 TL and appear as DOS peaks in the dI/dV spectrum. We identify spin-splitting and resonant topological surface states near E_F and -0.65 eV, which disappear at the step edges and in monolayer $NiTe_2$. Third, the QPI patterns exhibit a strong suppression within 140 ± 40 meV, which may be associated with the type-II Dirac point. Since the film samples can be more easily engineered via interface, thickness, etc., $NiTe_2$ film serves as a promising candidate to explore novel physics superior to its bulk counterparts.

ACKNOWLEDGMENTS

This work was financially supported by the National Key R&D Program of China (Grant No. 2022YFA1403100), Natural Science Foundation of China (Grants No. 52388201, No. 62074092, No. 52250402, No. 52072400, and No. 52025025), and Beijing Natural Science Foundation (Grant No. Z190010).

[1] S. Manzeli, D. Ovchinnikov, D. Pasquier, O. V. Yazyev, and A. Kis, 2D transition metal dichalcogenides, Nat. Rev. Mater. **2**, 17033 (2017).

[2] A. A. Soluyanov, D. Gresch, Z. Wang, Q. Wu, M. Troyer, X. Dai, and B. A. Bernevig, Type-II Weyl semimetals, Nature (London) **527**, 495 (2015).

[3] B. Yan and C. Felser, Topological materials: Weyl semimetals, Annu. Rev. Condens. Matter Phys. **8**, 337 (2017).

[4] N. P. Armitage, E. J. Mele, and A. Vishwanath, Weyl and Dirac semimetals in three-dimensional solids, Rev. Mod. Phys. **90**, 015001 (2018).

[5] M. S. Bahramy, O. J. Clark, B. J. Yang, J. Feng, L. Bawden, J. M. Riley, I. Markovic, F. Mazzola, V. Sunko, D. Biswas, S. P. Cooil, M. Jorge, J. W. Wells, M. Leandersson, T. Balasubramanian, J. Fujii, I. Vobornik, J. E. Rault, T. K. Kim, M. Hoesch *et al.*, Ubiquitous formation of bulk Dirac cones and topological surface states from a single orbital manifold in transition-metal dichalcogenides, Nat. Mater. **17**, 21 (2018).

[6] H.-J. Noh, J. Jeong, E.-J. Cho, K. Kim, B. I. Min, and B.-G. Park, Experimental realization of type-II Dirac fermions in a $PdTe_2$ superconductor, Phys. Rev. Lett. **119**, 016401 (2017).

[7] F. Fei, X. Bo, R. Wang, B. Wu, J. Jiang, D. Fu, M. Gao, H. Zheng, Y. Chen, X. Wang, H. Bu, F. Song, X. Wan, B. Wang, and G. Wang, Nontrivial Berry phase and type-II Dirac transport in the layered material $PdTe_2$, Phys. Rev. B **96**, 041201(R) (2017).

[8] M. Yan, H. Huang, K. Zhang, E. Wang, W. Yao, K. Deng, G. Wan, H. Zhang, M. Arita, H. Yang, Z. Sun, H. Yao, Y. Wu, S. Fan, W. Duan, and S. Zhou, Lorentz-violating type-II Dirac fermions in transition metal dichalcogenide $PtTe_2$, Nat. Commun. **8**, 257 (2017).

[9] A. Politano, G. Chiarello, B. Ghosh, K. Sadhukhan, C.-N. Kuo, C. S. Lue, V. Pellegrini, and A. Agarwal, 3D Dirac plasmons in the type-II Dirac semimetal $PtTe_2$, Phys. Rev. Lett. **121**, 086804 (2018).

[10] K. Zhang, M. Yan, H. Zhang, H. Huang, M. Arita, Z. Sun, W. Duan, Y. Wu, and S. Zhou, Experimental evidence for type-II Dirac semimetal in $PtSe_2$, Phys. Rev. B **96**, 125102 (2017).

[11] C. Xu, B. Li, W. Jiao, W. Zhou, B. Qian, R. Sankar, N. D. Zhigadlo, Y. Qi, D. Qian, F.-C. Chou, and X. Xu, Topological type-II Dirac fermions approaching the Fermi level in a transition metal dichalcogenide $NiTe_2$, Chem. Mater. **30**, 4823 (2018).

[12] B. Ghosh, D. Mondal, C.-N. Kuo, C. S. Lue, J. Nayak, J. Fujii, I. Vobornik, A. Politano, and A. Agarwal, Observation of bulk states and spin-polarized topological surface states in transition metal dichalcogenide Dirac semimetal candidate $NiTe_2$, Phys. Rev. B **100**, 195134 (2019).

[13] S. Mukherjee, S. W. Jung, S. F. Weber, C. Xu, D. Qian, X. Xu, P. K. Biswas, T. K. Kim, L. C. Chapon, M. D. Watson, J. B. Neaton, and C. Cacho, Fermi-crossing type-II Dirac fermions and topological surface states in $NiTe_2$, Sci. Rep. **10**, 12957 (2020).

[14] W. Zheng, R. Schonemann, S. Mozaffari, Y.-C. Chiu, Z. B. Goraum, N. Aryal, E. Manousakis, T. M. Siegrist, K. Wei, and L. Balicas, Bulk Fermi surfaces of the Dirac type-II semimetallic candidate $NiTe_2$, Phys. Rev. B **102**, 125103 (2020).

[15] M. Nurmamat, S. V. Eremeev, X. Wang, T. Yoshikawa, T. Kono, M. Kakoki, T. Muro, Q. Jiang, Z. Sun, M. Ye, and A. Kimura, Bulk Dirac cone and highly anisotropic electronic structure of $NiTe_2$, Phys. Rev. B **104**, 155133 (2021).

[16] T. Nguyen, N. Aryal, B. K. Pokharel, L. Harnagea, D. Mierstchin, D. Popovic, D. E. Graf, and K. Shrestha, Fermiology of the Dirac type-II semimetal candidates (Ni,Zr)Te_2 using de Haas–van Alphen oscillations, Phys. Rev. B **106**, 075154 (2022).

[17] J. Zhang and G. Q. Huang, The superconductivity and topological surface state of type-II Dirac semimetal $NiTe_2$, J. Phys.: Condens. Matter **32**, 205702 (2020).

[18] Z. Wang, Y. Sun, X.-Q. Chen, C. Franchini, G. Xu, H. Weng, X. Dai, and Z. Fang, Dirac semimetal and topological phase transitions in A_3Bi (A = Na, K, Rb), Phys. Rev. B **85**, 195320 (2012).

[19] Z. K. Liu, B. Zhou, Y. Zhang, Z. J. Wang, H. M. Weng, D. Prabhakaran, S.-K. Mo, Z. X. Shen, Z. Fang, X. Dai, Z. Hussain, and Y. L. Chen, Discovery of a three-dimensional topological Dirac semimetal, Na_3Bi, Science **343**, 864 (2014).

[20] Z. Wang, H. Weng, Q. Wu, X. Dai, and Z. Fang, Three-dimensional Dirac semimetal and quantum transport in Cd_3As_2, Phys. Rev. B **88**, 125427 (2013).

[21] Z. K. Liu, J. Jiang, B. Zhou, Z. J. Wang, Y. Zhang, H. M. Weng, D. Prabhakaran, S.-K. Mo, H. Peng, P. Dudin, T. Kim, M.

Hoesch, Z. Fang, X. Dai, Z. X. Shen, D. L. Feng, Z. Hussain, and Y. L. Chen, A stable three-dimensional topological Dirac semimetal Cd_3As_2, Nat. Mater. **13**, 677 (2014).

[22] S. Borisenko, Q. Gibson, D. Evtushinsky, V. Zabolotnyy, B. Buechner, and R. J. Cava, Experimental realization of a three-dimensional Dirac semimetal, Phys. Rev. Lett. **113**, 027603 (2014).

[23] M. Neupane, S.-Y. Xu, R. Sankar, N. Alidoust, G. Bian, C. Liu, I. Belopolski, T.-R. Chang, H.-T. Jeng, H. Lin, A. Bansil, F. Chou, and M. Z. Hasan, Observation of a three-dimensional topological Dirac semimetal phase in high-mobility Cd_3As_2, Nat. Commun. **5**, 3786 (2014).

[24] Q. Li, D. E. Kharzeev, C. Zhang, Y. Huang, I. Pletikosic, A. V. Fedorov, R. D. Zhong, J. A. Schneeloch, G. D. Gu, and T. Valla, Chiral magnetic effect in $ZrTe_5$, Nat. Phys. **12**, 550 (2016).

[25] M. Udagawa and E. J. Bergholtz, Field-selective anomaly and chiral mode reversal in type-II Weyl materials, Phys. Rev. Lett. **117**, 086401 (2016).

[26] M. Alidoust, K. Halterman, and A. A. Zyuzin, Superconductivity in type-II Weyl semimetals, Phys. Rev. B **95**, 155124 (2017).

[27] P. P. Ferreira, A. L. R. Manesco, T. T. Dorini, L. E. Correa, G. Weber, A. J. S. Machado, and L. T. F. Eleno, Strain engineering the topological type-II Dirac semimetal $NiTe_2$, Phys. Rev. B **103**, 125134 (2021).

[28] J. Shi, Y. Huan, M. Xiao, M. Hong, X. Zhao, Y. Gao, F. Cui, P. Yang, S. J. Pennycook, J. Zhao, and Y. Zhang, Two-dimensional metallic $NiTe_2$ with ultrahigh environmental stability, conductivity, and electrocatalytic activity, ACS Nano **14**, 9011 (2020).

[29] W.-X. Wang, K. Li, X. Dong, H. Xie, J. Qiu, C. Xu, K. Liu, J. Song, Y. Liu, K.-K. Bai, Y.-W. Wei, and X. Xu, Visualizing the atomic defects by scanning tunneling microscopy in the type-II Dirac semimetal $NiTe_2$, Phys. Scr. **98**, 015020 (2023).

[30] B. T. Blue, S. D. Lough, D. Le, J. E. Thompson, T. S. Rahman, R. Sankar, and M. Ishigami, Scanning tunneling microscopy and spectroscopy of $NiTe_2$, Surf. Sci. **722**, 122099 (2022).

[31] H. Zheng, Y. Choi, F. Baniasadi, D. Hu, L. Jiao, K. Park, and C. Tao, Visualization of point defects in ultrathin layered 1*T*-$PtSe_2$, 2D Mater. **6**, 041005 (2019).

[32] K. Zhussupbekov, L. Ansari, J. B. McManus, A. Zhussupbekova, I. V. Shvets, G. S. Duesberg, P. K. Hurley, F. Gity, C. O. Coileain, and N. McEvoy, Imaging and identification of point defects in $PtTe_2$, npj 2D Mater. Appl. **5**, 14 (2021).

[33] G. Anemone, P. Casado Aguilar, M. Garnica, F. Calleja, A. Al Taleb, C.-N. Kuo, C. S. Lue, A. Politano, A. L. Vazquez de Parga, G. Benedek, D. Farias, and R. Miranda, Electron-phonon coupling in superconducting 1*T*-$PdTe_2$, npj 2D Mater. Appl. **5**, 25 (2021).

[34] P. Casado Aguilar, F. Calleja, C.-N. Kuo, C. S. Lue, B. Ghosh, A. Agarwal, A. Politano, A. L. Vazquez de Parga, R. Miranda, J. A. Silva-Guillen, and M. Garnica, Atomic-scale study of type-II Dirac semimetal $PtTe_2$ surface, J. Phys. Mater. **5**, 044003 (2022).

[35] J. Li, T. Joseph, M. Ghorbani-Asl, S. Kolekar, A. Krasheninnikov, and M. Batzill, Edge and point-defect induced electronic and magnetic properties in monolayer $PtSe_2$, Adv. Funct. Mater. **32**, 2110428 (2022).

[36] J. A. Hlevyack, L.-Y. Feng, M.-K. Lin, R. A. B. Villaos, R.-Y. Liu, P. Chen, Y. Li, S.-K. Mo, F.-C. Chuang, and T. C. Chiang, Dimensional crossover and band topology evolution in ultrathin semimetallic $NiTe_2$ films, npj 2D Mater. Appl. **5**, 40 (2021).

[37] B. Seredynski, Z. Ogorzalek, W. Zajkowska, R. Bozek, M. Tokarczyk, J. Suffczynski, S. Kret, J. Sadowski, M. Gryglas-Borysiewicz, and W. Pacuski, Molecular beam epitaxy of a 2D material nearly lattice matched to a 3D substrate: $NiTe_2$ on GaAs, Cryst. Growth Des. **21**, 5773 (2021).

[38] B. Zhao, W. Dang, Y. Liu, B. Li, J. Li, J. Luo, Z. Zhang, R. Wu, H. Ma, G. Sun, Y. Huang, X. Duan, and X. Duan, Synthetic control of two-dimensional $NiTe_2$ single crystals with highly uniform thickness distributions, J. Am. Chem. Soc. **140**, 14217 (2018).

[39] Y. Guo, L. Kang, Q. Zeng, M. Xu, L. Li, Y. Wu, J. Yang, Y. Zhang, X. Qi, W. Zhao, Z. Zhang, and Z. Liu, Two-step chemical vapor deposition synthesis of $NiTe_2$-MoS_2 vertical junctions with improved MoS_2 transistor performance, Nanotechnol. **32**, 235204 (2021).

[40] W. Bensch, W. Heid, M. Muhler, S. Jobic, R. Brec, and J. Rouxel, Anionic polymeric bond in nickel ditelluride crystal structure experimental theoretical band structure, J. Solid State Chem. **121**, 87 (1996).

[41] L. Noren, V. Ting, R. Withers, and G. Van Tendeloo, An electron and x-ray diffraction investigation of $Ni_{1+x}Te_2$ and $Ni_{1+x}Se_2CdI_2$/NiAs type solid solution phases, J. Solid State Chem. **161**, 266 (2001).

[42] X. Zhao, P. Song, C. Wang, A. C. Riis-Jensen, W. Fu, Y. Deng, D. Wan, L. Kang, S. Ning, J. Dan, T. Venkatesan, Z. Liu, W. Zhou, K. S. Thygesen, X. Luo, S. J. Pennycook, and K. P. Loh, Engineering covalently bonded 2D layered materials by self-intercalation, Nature (London) **581**, 171 (2020).

[43] M.-Q. Ren, S. Han, J.-Q. Fan, L. Wang, P. Wang, W. Ren, K. Peng, S. Li, S.-Z. Wang, F.-W. Zheng, P. Zhang, F. Li, X. Ma, Q.-K. Xue, and C.-L. Song, Semiconductor-metal phase transition and emergent charge density waves in 1*T*-ZrX_2 (X = Se, Te) at the two-dimensional limit, Nano Lett. **22**, 476 (2022).

[44] L. Bürgi, O. Jeandupeux, H. Brune, and K. Kern, Probing hot-electron dynamics at surfaces with a cold scanning tunneling microscope, Phys. Rev. Lett. **82**, 4516 (1999).

[45] S. Crampin, J. Kroger, H. Jensen, and R. Berndt, Phase coherence length and quantum interference patterns at step edges, Phys. Rev. Lett. **95**, 029701 (2005).

[46] C.-L. Song, L. Wang, K. He, S.-H. Ji, X. Chen, X.-C. Ma, and Q.-K. Xue, Probing Dirac fermion dynamics in topological insulator Bi_2Se_3 films with a scanning tunneling microscope, Phys. Rev. Lett. **114**, 176602 (2015).

[47] T. Zhang, P. Cheng, X. Chen, J.-F. Jia, X. Ma, K. He, L. Wang, H. Zhang, X. Dai, Z. Fang, X. Xie, and Q.-K. Xue, Experimental demonstration of topological surface states protected by time-reversal symmetry, Phys. Rev. Lett. **103**, 266803 (2009).

[48] Z. Feng, J. Si, T. Li, H. Dong, C. Xu, J. Yang, Z. Zhang, K. Wang, H. Wu, Q. Hou, J.-J. Xing, S. Wan, S. Li, W. Deng, J. Feng, A. Pal, F. Chen, S. Hu, J.-Y. Ge, C. Dong *et al.*, Evidences for pressure-induced two-phase superconductivity and mixed structures of $NiTe_2$ and NiTe in type-II Dirac semimetal $NiTe_{2-x}$ ($x = 0.38 \pm 0.09$) single crystals, Mater. Today Phys. **17**, 100339 (2021).

[49] M. Qi, C. An, Y. Zhou, H. Wu, B. Zhang, C. Chen, Y. Yuan, S. Wang, Y. Zhou, X. Chen, R. Zhang, and Z. Yang,

Pressure-driven Lifshitz transition in type-II Dirac semimetal $NiTe_2$, Phys. Rev. B **101**, 115124 (2020).

[50] B. S. de Lima, R. R. de Cassia, F. B. Santos, L. E. Correa, T. W. Grant, A. L. R. Manesco, G. W. Martins, L. T. F. Eleno, M. S. Torikachvili, and A. J. S. Machado, Properties and superconductivity in Ti-doped $NiTe_2$ single crystals, Solid State Commun. **283**, 27 (2018).

[51] M. Mandal and R. P. Singh, Emergent superconductivity by Re doping in type-II Weyl semimetal $NiTe_2$, J. Phys.: Condens. Matter **33**, 135602 (2021).

[52] M.-Q. Ren, S.-Z. Wang, S. Han, C.-L. Song, X.-C. Ma, and X. Qi-Kun, Tuning the electronic states and superconductivity in alkali fulleride films, AAPPS Bull. **32**, 1 (2022).

[53] M.-Q. Ren, S. Han, S.-Z. Wang, J.-Q. Fan, C.-L. Song, X.-C. Ma, and Q.-K. Xue, Direct observation of full-gap superconductivity and pseudogap in two-dimensional fullerides, Phys. Rev. Lett. **124**, 187001 (2020).

[54] F. Zheng, X.-B. Li, Y. Lin, L. Xiong, X. Chen, and J. Feng, Emergent superconductivity in two-dimensional $NiTe_2$ crystals, Phys. Rev. B **101**, 100505(R) (2020).